RSC Advances

ROYAL SOCIETY OF CHEMISTRY

www.rsc.org/advances

Facile large-scale synthesis of Au-Pt alloyed nanowire networks as efficient electrocatalysts for methanol oxidation and oxygen reduction reactions

Pei Song,† Shan-Shan Li,† Li-Li He, Jiu-Ju Feng, Liang Wu, Shu-Xian Zhong, Ai-Jun Wang*

College of Geography and Environmental Science, College of Chemistry and Life Science, Zhejiang Normal University, Jinhua 321004, China

† These authors contributed equally to this work.

**Corresponding Author: ajwang@zjnu.cn (A.J. Wang); Tel./Fax: +86 579 82282269.*

Abstract

In this work, bimetallic Au-Pt alloyed nanowire networks (AuPt NNs) were facilely synthesized by a simple and rapid one-pot wet-chemical method on a large-scale, using *N*-methylimidazole as a structure-directing agent and a weak stabilizing agent. The surface of AuPt NNs was clean owing to the easy removal of the adsorbed *N*-methylimidazole. The control experiments demonstrated that the morphologies of AuPt NNs were strongly correlated with the amount of *N*-methylimidazole and reaction temperature. The formation mechanism included the four-staged growth processes: rapid nucleation, selective adsorption, π-π induced assembly, and oriented attachment growth. The as-synthesized AuPt NNs exhibited enhanced elctrocatalytic activity and improved stability for methanol oxidation reaction (MOR) and oxygen reduction reaction (ORR) as compared to commercial Pt black and individual Pt nanoparticles.

Keywords: Bimetallic alloy; Nanowire networks; *N*-methylimidazole; Methanol oxidation reaction; Oxygen reduction reaction

1 Introduction

Fuel cells, such as direct methanol fuel cells, direct ethanol fuel cells, and alkaline fuel cells, have attracted significant attention over the past few decades, thanks to their high power density and energy-conversion efficiency, as well as zero and/or low emission of pollutants.[1, 2] Platinum (Pt) is widely used as a catalyst for electrooxidation of small organic fuels on the anode and oxygen reduction reaction (ORR) on the cathode in fuel cells, because of its superior catalytic activity. However, Pt is severely hindered from wide-spread commercialization because of its poor stability, weak poison resistance, and slow reaction kinetics.[3-5] To overcome these issues, extensive researches were carried out based on Pt-based bimetallic catalysts with controlled surface structures and compositions.[6, 7]

In recent years, tremendous progresses have been made on the design and construction of bimetallic nanostructures with improved catalytic, electrical and optical properties by adjusting the respective compositions.[8, 9] For instance, Pt-M (M = Au, Pd, Ru, and Fe) nanostructures confirmed highly improved catalytic performance toward ORR,[6, 10] methanol oxidation reaction (MOR),[11, 12] and formic acid oxidation reaction (FAOR)[13, 14] as compared to individual Pt catalysts.

It is well known that Au is unique in view of its inertness in bulk and its high catalytic activity at nanoscale level.[15] For instance, Au nanoparticles demonstrate superior electrocatalytic activity for CO oxidation.[15, 16] Therefore, AuPt alloy is expected to have better catalytic activity in comparison with single Pt and Au counterparts.[17, 18] Meanwhile, Pt catalysts can be efficiently stabilized in the presence

of neighboring Au atoms, which would modify Pt electronic structure and lower the d-band center.[18, 19] Hence, the poisoning problem of Pt catalysts can be solved via the design and construction of AuPt alloys to enhance the catalytic selectivity toward target molecules and decrease the deactivation rate for their commercial applications in fuel cells.[20-22]

The shape of a catalyst is tightly related with their catalytic performance, and thereby diverse PtAu nanocatalysts with different shapes have been synthesized, including particles,[23] cubes,[24] wires,[20] rods,[25] core-shells,[26] multipods,[27] urchins,[28] and dendrites.[21] Among them, PtAu wires have improved catalytic activity and long-term durability in fuel cells due to their unique anisotropic nature, especially the enrichment of the low energy (111) and (100) planes and the minimization of low-coordination defect sites.[29, 30]

Generally, metallic nanocrystals with unique morphologies were prepared by controlling the anisotropic growth with the assistance of capping agents (e.g., polymer, dendrimer, and ligand) or based on the intrinsic growth habits of the crystals, in which the introduced capping agents have strong interactions with the metal precursors, which can tune surface energy and particle dispersity.[9] For example, Xia's group prepared Ag nanowires in the presence of poly(vinyl pyrrolidone) using Pt nanoparticles as seeds.[31] Dong and co-workers fabricated PtPd and PdAu nanowires by using Te nanowires as the sacrificial template and the reducing agent.[20] Song et al. synthesized Pt nanowire networks with the assistance of ceintyltrimethylammonium bromide as a soft template in a two-phase water-chloroform system.[32] Nevertheless,

the as-established methods suffer from time-consuming and complicated reaction procedures, which seriously limit their development and commercialization.[33]

Moreover, the use of capping agents might eventually block the mass transport and electron transfer of reactant molecules, which severely affects its catalytic activity in practical applications.[34] In addition, organic solvents, such as trichloromethane and toluene, are usually used previously in the synthesis of nanowire networks, which is a great threat to human beings' health.[32, 35] Thus, it is necessary to develop a facile one-pot green method for shape-controlled synthesis of surface-clean nanowire networks on a large scale, using small molecules instead of polymers or surfactants.

In this report, Au-Pt alloy nanowire networks (AuPt NNs) were facilely prepared in the presence of *N*-methylimidazole by a rapid (within 3 min), seed-less, and one-pot wet-chemical method. The electrocatalytic activity of AuPt NNs was investigated in some detail, using MOR and ORR as model systems.

2 Experimental sections

2.1 Chemicals

Chloroauric acid ($HAuCl_4$), chloroplatinic acid (H_2PtCl_6), *N*-methylimidazole, ascorbic acid (AA), methanol and Pt black were purchased from Aladdin Chemistry Co. Ltd (Shanghai, China). All the other reagents were analytical grade and used as received without further purification.

2.2 Synthesis of AuPt NNs

In a typical synthesis, 100 μL of 24.3 mM $HAuCl_4$, 65 μL of 38.6 mM H_2PtCl_6, and 20 μL of *N*-methylimidazole were put into 8 mL of water under vigorous stirring in a water-bath with the temperature of 80 °C, followed by the drop-wise addition of 2 mL of freshly-prepared AA solution (0.1 M). Afterward, the mixture was kept at 80 °C for another 3 min under stirring. The resulting products were collected by centrifugation and thoroughly washed with water and ethanol, ensuring the complete removal of *N*-methylimidazole molecules from the product, and finally dried at 60 °C in vacuum for further characterization.

Control experiments were performed by varying the precursors, the amount of *N*-methylimidazole, and the reaction temperature, while the other experimental conditions were kept constant.

2.3 Characterization

The size and shape of the products were examined by transmission electron microscopy (TEM) and high-resolution TEM (HR-TEM) images by using a JEOL-2100F transmission electron microscope operated at 200 kV equipped with selective area electron diffraction (SAED). High-angle annular dark-field scanning transmission electron microscopy (HAADF-STEM) images, element analysis mapping, and energy dispersive spectroscopy (EDS) line scans were all taken on a HITACHI S-5500 microscope operated at 30 kV. To characterize the crystallinity of the products, power X-ray diffraction (XRD) experiments were performed on a Philips PW3040/60 diffractometer with Cu Kα radiation (λ = 0.15418 nm). X-ray

photoelectron spectroscopy (XPS) measurements were conducted on a Themo SCIENTIFIC ESCALAB 250 spectrometer.

2.4 Electrochemical measurements

All the electrochemical experiments were performed on a CHI 660B electrochemical workstation (CH Instruments, Chenhua Co., Shanghai, China). A standard three-electrode system was used, which consisted of a platinum wire as the auxiliary electrode, a saturated calomel electrode (SCE) as the reference electrode, and a bare or modified glass carbon electrode (GCE, 3 mm in diameter) as the working electrode. Rotating disk electrode test was performed on a MODEL 616 Rotating Disk Electrode with a glass carbon rotating disk electrode (RDE, 4 mm in diameter). All the potentials in this study were reported with respect to SCE. All of the electrochemical measurements were conducted at room temperature.

For typical preparation of AuPt NNs modified electrode, 1 mg of the sample was dispersed into 1 mL water by ultrasonication to form a homogeneous suspension. Then, 6 and 20 μL of the suspension were casted on the GCE and RDE, and dried in air. Next, 5 and 10 μL of Nafion (0.05 %) was coated on the electrode surfaces and dried naturally. The loadings of the catalysts on the electrode surfaces are around 0.08 and 0.16 mg cm^{-2}, respectively. For comparison, Pt black, Au nanoparticles, and Pt nanoparticles modified electrodes were prepared with the similar procedures.

Cyclic voltammetry (CV) measurements were performed in 0.5 M H_2SO_4 at a scan rate of 50 mV s^{-1}. The electrochemically active surface area (ECSA) of the

catalyst modified electrode was calculated by measuring the charges collected in the hydrogen adsorption/desorption region after double-layer correction and assuming a value of 210 μC cm^{-2} for the adsorption of a hydrogen monolayer.[36] For MOR, CV and chronoamperometry experiments were conducted in 0.5 M H_2SO_4 containing 1.0 M methanol. And CO-stripping was performed in 0.5 M H_2SO_4 at 50 mV s^{-1}.

All the ORR measurements were carried out in O_2-saturated 0.1 M KOH. The polarization curves were obtained by sweeping the potential from 0.2 to –0.7 V at 10 mV s^{-1} with the rotation rate of 1600 rpm. The current density (j) was normalized in reference to the geometric area of RDE or GCE. Based on the ORR polarization curves, the kinetic current density (j_k) was calculated according to the Koutecky-Levich equation, which can be described as below (1-2):[5, 6, 29]

$$\frac{1}{j} = \frac{1}{j_k} + \frac{1}{j_d} \quad (1)$$

$$j_d = 0.62nFC_0D_0^{2/3}v^{-1/6}\omega^{1/2} \quad (2)$$

where j is the measured current density, j_d is the diffusion-limited current density, n is the electron transfer number, F is the Faraday constant (96485 C mol^{-1}), C_0 is the bulk concentration of O_2 (1.2×10^{-6} mol cm^{-3}), D_0 is the diffusion coefficient of O_2 (1.9×10^{-5} cm^2 s^{-1}), v is the kinematic viscosity of the electrolyte (0.01 cm^2 s^{-1}), and ω is the angular velocity ($\omega = 2\pi N$, N is the linear rotation speed). As a result, the n value can be determined from the plot of the j against the square root of the electrode rotation rate ($\omega^{1/2}$). The accelerated durability test was conducted in O_2-saturated 0.1 M KOH at 10 mV s^{-1} with the rotation rate of 1600 rpm.

3 Results and discussion

3. 1 Characterization

The structure features of the typical product were investigated firstly by TEM and HR-TEM analysis. As depicted in Fig. 1A and B, there are a variety of AuPt wires with the average diameter of 10 nm that are interconnected to form three-dimensional networks. HR-TEM images provide more detailed structural information of AuPt NNs (Fig. 1C and D). The well-resolved lattice fringes are clearly observed in the whole nanowires, with the inter-planar spacing distance of 0.235 nm indexed to the (111) lattice spacing of the face-centered cubic (fcc) AuPt alloy.[6] Furthermore, HR-TEM images confirm that the long axis of the nanowires is always perpendicular to the (111) planes, indicating the preferential growth of AuPt NNs along the (111) directions. Additionally, the SAED patterns taken from the marked positions demonstrate good crystallinity of AuPt NNs (Fig. 1E).

The XRD pattern of AuPt NNs (Fig. 1F, curve a) shows four characteristic diffraction peaks at 38.61, 44.92, 65.52, and 78.61, corresponding to the (111), (200), (220), and (311) planes of the fcc Au/Pt, respectively. These diffraction peaks are located between bulk Au (curve b, JCPDS No. 04-0784) and Pt (curve c, JCPDS No. 04-0802), further reflecting the formation of AuPt alloy.

The HAADF-STEM-EDS mapping reveals that Au and Pt are uniformly distributed in AuPt NNs (Fig. 2A-C). Meanwhile, the corresponding cross-sectional compositional line scanning profiles further manifest the homogeneous distribution of Au and Pt, indicating the alloy structures of the nanowires (Fig. 2D). The EDS pattern reveals that Au and Pt are predominant species, and the molar ratio of Au to Pt is

about 3:1 (Fig. S1, ESI, Electronic Supplementary Information).

It is known that the catalytic activity of a catalyst is closely associated with its surface compositions.[37] Therefore, we checked the surface compositions of AuPt NNs by XPS.[38] The predominant peaks at 74, 85, 285, and 532 eV are well assigned to Pt, Au, C, and O elements in the survey XPS spectrum, respectively (Fig. S2A, ESI). The peaks of C and O elements come from the conductive adhesive for fixing the sample during XPS measurements. More importantly, the peak of N 1s located at around 399 eV is not observed in the XPS survey spectrum, which indicates the complete removal of *N*-methylimidazole from the surface of AuPt NNs.

Fig. S2B and C (ESI) show the high-resolution XPS spectra of Au 4f and Pt 4f for AuPt NNs. The Au $4f_{7/2}$ and Au $4f_{5/2}$ peaks detected at 83.9 and 87.6 eV are attributed to metallic Au^0.[39] The two pairs of doubles at 70.7 and 74.1 eV; 71.5 and 75.0 eV are assigned to Pt^0 and Pt^{2+}, respectively.[11] The existence of Pt^{2+} is ascribed to the incomplete reduction of $PtCl_6^{2-}$ in this synthesis, along with the easy oxidation of the surface Pt to form Pt oxide under ambient conditions.[40] Furthermore, the binding energy of Au shifts positively, while Pt displays a negative shift for AuPt NNs in comparison with Au and Pt nanoparticles (Au^0: 83.2 and 86.9 eV; Pt^0: 71.2 and 74.6 eV, Fig. S3, ESI). These results indicate a slight change occurred in the electronic structure of Au and Pt.[41] Additionally, by estimating from the relative peak intensity, the molar ratio of Au to Pt is around 3:1, which is well consistent with the EDS data.

3. 2 Formation mechanism

To have a deep insight into the formation mechanism of AuPt NNs, a series of control experiments were preformed. The only use of $HAuCl_4$ as a precursor produces Au nanoparticles with serious agglomeration (Fig. S4A, ESI). On the contrary, the presence of H_2PtCl_6 yields a few small Pt nanoparticles (Fig. S4B, ESI). Besides, the absence of *N*-methylimidazole in the control experiments induces the formation of irregular solid nanoparticles (Fig. 3A).

Impressively, insufficient *N*-methylimidazole leads to the emergence of nanowires with poor quality (Fig. 3B), while the nanowires become aggregated, thin, and short in the case of excessive *N*-methylimidazole (Fig. 3C and D). Therefore, *N*-methylimidazole with appropriate amount plays a critical role, owing to its selective binding on the specific crystal surfaces during the growth process.[3, 42, 43]

Furthermore, the reaction temperature plays an important role in the synthesis of AuPt NNs. Low temperature (60 ºC) makes the nanowires thick with agglomeration (Fig. S5A, ESI), and much lower temperature (40 ºC) induces the formation of sheet-like structures with severe aggregation (Fig. S5B, ESI). Decreasing the reaction temperature causes the increase of the viscosity in the reaction media, and the decreased molecular disordered movement and diffusion rate.[44, 45] Thus, high temperature facilitates the formation of well-defined AuPt NNs with high yield.

As well known, semiconductor and oxide nanoparticles can grow into nanowires, mainly driving by magnetic dipole moments and electric dipole moments.[46, 47] However, the driving force for oriented attachment is not very clear in metal nanoparticles that have no permanent dipole moments. Thus, the oriented attachment

growth is generally ascribed to the specific binding of a capping agent onto certain crystal surfaces. For example, bases preferentially adsorb onto the Pt (100) and Pt (110) crystal planes, facilitating the growth of Pt nanostructures along the (111) directions.[3, 48]

The formation mechanism of AuPt NNs can be described by the four-staged growth model: rapid nucleation, selective adsorption, π-π induced assembly, and oriented attachment growth for nanowire networks. This hypothesis is well demonstrated by the time-dependent control experiments (Fig. S6, ESI), as described in Fig. 4. At the very early stage, $AuCl_4^-$ and $PtCl_6^{2-}$ are quickly reduced to form metallic Au and Pt atoms upon the addition of AA, owing to the strong reducing property of AA at high temperature.[49] Then, the newly formed Au and Pt atoms quickly fuse together to form small AuPt nuclei. The adjacent *N*-methylimidazole molecules can rapidly and selectively adsorb on the low energy AuPt crystal (100) and (110) planes as the directing agent, resulting in the predominant formation of AuPt NNs along the (111) directions,[3, 42, 43, 50] as strongly confirmed by the associated HR-TEM images (Fig. 1C and D). Meanwhile, the π-π interactions among imidazole rings in *N*-methylimidazole would further promote the coalescence of AuPt nuclei and oriented growth along the (111) planes, inducing the formation of AuPt NNs.[51, 52]

3. 3 Electrochemical properties

The CV curves of AuPt NNs (curve a), Pt black (curve b), and Pt nanoparticles (curve c) modified electrodes were recorded in 0.5 M H_2SO_4 at a scan rate of 50 mV

s^{-1} (Fig. S7A, ESI). There are three distinctive potential regions associated with the hydrogen adsorption/desorption process ($H + e^- = H_{upd}$) in the range from –0.2 to 0 V, double layer region from 0 to 0.2 V, and reversible adsorption of OH_{ad} ($2H_2O = OH_{ad} + H_3O^+ + e^-$) beyond 0.2 V, where H_{upd} and OH_{ad} refer to the under-potentially deposited hydrogen and the adsorbed oxygenated species, respectively.[53] The specific ECSA (the ECSA per unit weight of metal) of AuPt NNs, Pt black, and Pt nanoparticles modified electrodes are determined to be 50.4, 30.8, and 15.2 $m^2\ g^{-1}$, respectively. Besides, the CV curve of Au nanoparticles modified electrode in 0.5 M H_2SO_4 was shown in Fig. S7B (ESI). The specific ECSA of Au nanoparticles is calculated to be 17.6 $m^2\ g^{-1}$, by evaluating the amount of the charges consumed during the reduction of the surface Au oxide monolayer.[54] It means that AuPt NNs provide a relatively larger ECSA because of their unique interconnected nanostructures.

The electrocatalytic performance of AuPt NNs modified electrode for MOR was investigated in 0.5 M H_2SO_4 at 50 mV s^{-1}. In the CV curves (Fig. 5A), there are two distinguished anodic peaks which are typical MOR features during the positive and negative sweeps. The corresponding peak current density is 49.2 mA cm^{-2} in the positive scan, which is 2.2 and 2.7 times higher than those of Pt black (22.0 mA cm^{-2}) and Pt nanoparticles (18.5 mA cm^{-2}). Besides, the onset potential occurs at 0.02 V for AuPt NNs, which is negative than those of Pt black (0.05 V) and Pt nanoparticles (0.08 V).

Mass activity and specific activity were estimated to further examine the

catalytic abilities of the above catalysts,[29, 53] which are obtained by normalizing the positive peak current to the metal loading and the ECSA, respectively. Fig. 5B shows the mass activity and specific activity of AuPt NNs, Pt black, and Pt nanoparticles modified electrodes. These results clearly demonstrate the enhanced catalytic activity of AuPt NNs.

The stability of a catalyst is usually recognized as one of the most critical issues to be addressed before the commercialization in fuel cells.[55, 56] The catalytic stability of AuPt NNs for MOR is investigated by chronoamperometry. As shown in Fig. 5C, the oxidation currents decrease continuously for AuPt NNs, Pt black, and Pt nanoparticles modified electrodes, possibly due to the formation of intermediate and poison species such as CO_{ads}, CH_3OH_{ads}, and CHO_{ads} during methanol oxidation.[57] After long-time operation, although the current densities gradually decay for all the catalysts, higher current density is still remained for AuPt NNs in contrast with the other catalysts. Meanwhile, a slight negative shift of the CO stripping potential is observed for AuPt NNs in comparison with Pt black, revealing that AuPt NNs facilitate CO oxidation (Fig. S8, ESI). In addition, the ECSA of AuPt NNs and commercial Pt black could be also calculated from the CO stripping experiment, by measuring the charges collected in the CO oxidation region and assuming a value of 420 μC cm^{-2} for the oxidizing of a monolayer adsorbed CO on a catalyst surface.[6] The $ECSA_{CO}$ of AuPt NNs and commercial Pt black are calculated to be 47.4 and 28.6 m^2 g^{-1}, which is similar with the $ECSA_H$ and the reports in literature.[33] All of these results verify the higher catalytic activity of AuPt NNs for their unique interconnected

structure toward MOR.

We further evaluated the catalytic performance of AuPt NNs modified electrodes in O_2-saturated 0.1 M KOH at 10 mV s^{-1} with a rotation rate of 1600 rpm (Fig. 6A). For all the catalysts, the diffusion-limited current region ranges from –0.7 to –0.2 V, whereas a mixed kinetics-diffusion control region occurs between –0.2 and 0.1 V. The onset potential (0.10 V) and half-wave potential (–0.18 V) on AuPt NNs modified electrode are positive than those of Pt black (0.08 V and –0.19 V), Au nanoparticles (–0.17 and –0.36 V), and Pt (–0.13 and –0.232 V) nanoparticles modified electrodes under the same conditions, owing to the long segments of the (111) planes on the nanowire surface. Also, the onset potential and half-wave potential of AuPt NNs modified electrode both have slight positive shifts for ORR as compared to the Pt-based catalysts in the literature.[6, 29, 58]

The diffusion-limited current density is 5.08 mA cm^{-2} at –0.7 V for AuPt NNs, which is much higher than Pt black (4.99 mA cm^{-2}), Au nanoparticles (2.49 mA cm^{-2}), and Pt nanoparticles (4.64 mA cm^{-2}) modified electrodes. Furthermore, AuPt NNs modified electrode also shows the highest current density at the kinetic diffusion controlled regions. It is ascribed to the seriously aggregation of Pt black (Fig. S9, ESI) and Pt nanoparticles (Fig. S4B, ESI).

We also compare the mass kinetic activity and specific kinetic activity of the catalysts (Fig. 6B). The mass kinetic and specific kinetic current densities of AuPt NNs are calculated to be 103 mA mg^{-2} and 0.62 mA cm^{-2}, which are much higher than those of Pt nanoparticles (74 mA mg^{-2} and 0.30 mA cm^{-2}) and commercial Pt

black (92 mA mg^{-2} and 0.31 mA cm^{-2}). All of the results indicate the improved ORR activity of AuPt NNs, thanks to the larger exposed active sites and the improved mass-transport properties of nanowire networks.[59, 60]

To further determine the electrocatalytic activity of AuPt NNs modified electrode for ORR, the steady-state polarization curves were recorded at 10 mV s^{-1} over a range of rotation rates of 100-2500 rpm (Fig. 7A). Fig. 7B shows the corresponding Koutecky-Levich plots. According to the respective slope values, the electron transfer number involved in ORR is deduced to be 3.8~4.0 for AuPt NNs, which is in good accordance with the theoretical value,[3, 61] revealing that ORR is mainly dominated by a four-electron transfer pathway.

The accelerated durability test was conducted in O_2-saturated 0.1 M KOH at a scan rate of 10 mV s^{-1} with a rotation rate of 1600 rpm. After 500 cycles, the catalytic activity of AuPt NNs modified electrode shows only 10 mV degradation in half-wave potential ($E_{1/2}$), as well as almost constant current density (Fig. 7C).

In general, Pt catalysts have abundant surface defect sites which originate from the local differences in coordination geometry and surface energy of Pt atoms.[62] The existence of the defect sites exhibits slow kinetics and catalytic inhibition for ORR, owing to their preferential adsorption of surface OH groups on the defect sites.[62, 63] Besides, the preferential display of low energy crystal facets of PtAu wires contribute to an increase in the catalytic activity for ORR.[29] Thus, the improved catalytic activity of AuPt NNs is attributed to (1) the enlarged exposed active sites on AuPt nanwires,[62] (2) the clean surface and low energy crystal planes (e.g. the Au/Pt (111) planes), (3)

the changes in the electronic structure and d-band center as Au is doped by Pt,[19] and (4) the unique interconnected nanowire networks that facilitate the electron transport and methanol/oxygen diffusion,[64]

4 Conclusions

In conclusion, a simple and rapid one-pot wet-chemical method was developed to prepare surface-clean AuPt NNs on a large-scale, without any pre-made seed, polymer or template, in which *N*-methylimidazole served as a structure-directing agent and a weak stabilizing agent. The formation mechanism of AuPt NNs was described as the four-staged growth processes involved including rapid nucleation, selective adsorption, π-π induced assembly, and oriented attachment growth. The as-prepared AuPt NNs exhibited superior catalytic activity and better stability toward MOR and ORR in comparison with Pt black and Pt nanoparticles. The improved durability of AuPt NNs was ascribed to their unique interconnected structures. The present study provided a simple and effective approach for synthesis of other bimetallic catalysts with controllable morphologies and highly catalytic properties with the assistance of small molecules instead of polymer or surfactant.

Acknowledgements

This work was financially supported by the National Natural Science Foundation of China (Nos. 21475118, 21175118, and 21275130).

References

1 T. Yajima, H. Uchida and M. Watanabe, *J. Phys. Chem. B*, 2004, **108**, 2654-2659.

2 J.-J. Lv, S.-S. Li, J.-N. Zheng, A.-J. Wang, J.-R. Chen and J.-J. Feng, *Int. J. Hydrogen Energy*, 2014, **39**, 3211-3218.

3 L. Ruan, E. Zhu, Y. Chen, Z. Lin, X. Huang, X. Duan and Y. Huang, *Angew. Chem. Int. Ed.*, 2013, **52**, 12577-12581.

4 A.-X. Yin, X.-Q. Min, Y.-W. Zhang and C.-H. Yan, *J. Am. Chem. Soc.*, 2011, **133**, 3816-3819.

5 S.-S. Li, J.-J. Lv, L.-N. Teng, A.-J. Wang, J.-R. Chen and J.-J. Feng, *ACS Appl. Mat. Interfaces*, 2014, **6**, 10549-10555.

6 J.-N. Zheng, S.-S. Li, X. Ma, F.-Y. Chen, A.-J. Wang, J.-R. Chen and J.-J. Feng, *J. Mater. Chem. A*, 2014, **2**, 8386-8395.

7 H. Zhang, M. Jin and Y. Xia, *Chem. Soc. Rev.*, 2012, **41**, 8035-8049.

8 S. Guo and E. Wang, *Nano Today*, 2011, **6**, 240-264.

9 H. You, S. Yang, B. Ding and H. Yang, *Chem. Soc. Rev.*, 2012, **42**, 2880-2904.

10 G. Fu, K. Wu, J. Lin, Y. Tang, Y. Chen, Y. Zhou and T. Lu, *J. Phys. Chem. C*, 2013, **117**, 9826-9834.

11 S.-S. Li, J.-N. Zheng, X. Ma, Y.-Y. Hu, A.-J. Wang, J.-R. Chen and J.-J. Feng, *Nanoscale*, 2014, **6**, 5708-5713.

12 Y. Peng, C. Liu, C. Pan, L. Qiu, S. Wang and F. Yan, *ACS Appl. Mat. Interfaces*, 2013, **5**, 2752-2760.

13 S. Zhang, Y. Shao, H.-g. Liao, J. Liu, I. A. Aksay, G. Yin and Y. Lin, *Chem. Mater.*,

2011, **23**, 1079-1081.

14 W. Chen, J. Kim, S. Sun and S. Chen, *Langmuir*, 2007, **23**, 11303-11310.

15 Y. Hu, H. Zhang, P. Wu, H. Zhang, B. Zhou and C. Cai, *Phys. Chem. Chem. Phys.*, 2011, **13**, 4083-4094.

16 T. F. Jaramillo, S.-H. Baeck, B. R. Cuenya and E. W. McFarland, *J. Am. Chem. Soc.*, 2003, **125**, 7148-7149.

17 S. Guo, L. Wang, S. Dong and E. Wang, *J. Phys. Chem. C*, 2008, **112**, 13510-13515.

18 M. Cao, D. Wu and R. Cao, *ChemCatChem*, 2014, **6**, 26-45.

19 J. Zhang, K. Sasaki, E. Sutter and R. R. Adzic, *Science*, 2007, **315**, 220-222.

20 C. Zhu, S. Guo and S. Dong, *Adv. Mater.*, 2012, **24**, 2326-2331.

21 J. Wang, D. F. Thomas and A. Chen, *Chem. Commun.*, 2008, 5010-5012.

22 Y. Yamauchi, A. Tonegawa, M. Komatsu, H. Wang, L. Wang, Y. Nemoto, N. Suzuki and K. Kuroda, *J. Am. Chem. Soc.*, 2012, **134**, 5100-5109.

23 J. Xu, T. Zhao, Z. Liang and L. Zhu, *Chem. Mater.*, 2008, **20**, 1688-1690.

24 H. Li, H. Wu, Y. Zhai, X. Xu and Y. Jin, *ACS Catal.*, 2013, **3**, 2045-2051.

25 X. Zhong, H. Yu, X. Wang, L. Liu, Y. Jiang, L. Wang, G. Zhuang, Y. Chu, X. Li and J.-g. Wang, *ACS Appl. Mat. Interfaces*, 2014, **6**, 13448-13454.

26 N. C. Bigall, T. Härtling, M. Klose, P. Simon, L. M. Eng and A. Eychmüller, *Nano Lett.*, 2008, **8**, 4588-4592.

27 X. Teng and H. Yang, *Nano Lett.*, 2005, **5**, 885-891.

28 H. You, F. Zhang, Z. Liu and J. Fang, *ACS Catal.*, 2014, **4**, 2829-2835.

29 J. Xu, G. Fu, Y. Tang, Y. Zhou, Y. Chen and T. Lu, *J. Mater. Chem.*, 2012, **22**, 13585-13590.

30 C. Zhu, S. Guo and S. Dong, *J. Mater. Chem.*, 2012, **22**, 14851-14855.

31 Y. Sun, Y. Yin, B. T. Mayers, T. Herricks and Y. Xia, *Chem. Mater.*, 2002, **14**, 4736-4745.

32 Y. Song, R. M. Garcia, R. M. Dorin, H. Wang, Y. Qiu, E. N. Coker, W. A. Steen, J. E. Miller and J. A. Shelnutt, *Nano Lett.*, 2007, **7**, 3650-3655.

33 X. Yu, D. Wang, Q. Peng and Y. Li, *Chem.–Eur. J.*, 2013, **19**, 233-239.

34 X.-R. Li, X.-L. Li, M.-C. Xu, J.-J. Xu and H.-Y. Chen, *J. Mater. Chem. A*, 2014, **2**, 1697-1703.

35 G. Ramanath, J. D'Arcy-Gall, T. Maddanimath, A. V. Ellis, P. G. Ganesan, R. Goswami, A. Kumar and K. Vijayamohanan, *Langmuir*, 2004, **20**, 5583-5587.

36 B. Lim, M. Jiang, P. H. C. Camargo, E. C. Cho, J. Tao, X. Lu, Y. Zhu and Y. Xia, *Science*, 2009, **324**, 1302-1305.

37 D.-B. Huang, Q. Yuan, H.-H. Wang and Z.-Y. Zhou, *Chem. Commun.*, 2014, **50**, 13551-13554.

38 Y.-J. Deng, N. Tian, Z.-Y. Zhou, R. Huang, Z.-L. Liu, J. Xiao and S.-G. Sun, *Chem. Sci.*, 2012, **3**, 1157-1161.

39 F. Li, Y. Guo, R. Li, F. Wu, Y. Liu, X. Sun, C. Li, W. Wang and J. Gao, *J. Mater. Chem. A*, 2013, **1**, 6579-6587.

40 L. Feng, F. Si, S. Yao, W. Cai, W. Xing and C. Liu, *Catal. Commun.*, 2011, **12**, 772-775.

41 J. Chai, F. Li, Y. Hu, Q. Zhang, D. Han and L. Niu, *J. Mater. Chem.*, 2011, **21**, 17922-17929.

42 B. Y. Xia, H. B. Wu, X. Wang and X. W. Lou, *Angew. Chem. Int. Ed.*, 2013, **52**, 12337-12340.

43 B. Y. Xia, H. B. Wu, Y. Yan, X. W. Lou and X. Wang, *J. Am. Chem. Soc.*, 2013, **135**, 9480-9485.

44 S.-W. Bain, Z. Ma, Z.-M. Cui, L.-S. Zhang, F. Niu and W.-G. Song, *J. Phys. Chem. C*, 2008, **112**, 11340-11344.

45 W. Wang, Y. Han, M. Gao and Y. Wang, *CrystEngComm*, 2013, **15**, 2648-2656.

46 N. Pradhan, H. Xu and X. Peng, *Nano Lett.*, 2006, **6**, 720-724.

47 Z. Tang, N. A. Kotov and M. Giersig, *Science*, 2002, **297**, 237-240.

48 X. Yu, D. Wang, Q. Peng and Y. Li, *Chem.–Eur. J.*, 2013, **19**, 233-239.

49 S. W. Kang, Y. W. Lee, Y. Park, B.-S. Choi, J. W. Hong, K.-H. Park and S. W. Han, *ACS Nano*, 2013, **7**, 7945-7955.

50 M. Chen, B. Wu, J. Yang and N. Zheng, *Adv. Mater.*, 2012, **24**, 862-879.

51 K. E. Gutowski, V. A. Cocalia, S. T. Griffin, N. J. Bridges, D. A. Dixon and R. D. Rogers, *J. Am. Chem. Soc.*, 2007, **129**, 526-536.

52 J.-J. Feng, Z.-Y. Lv, S.-F. Qin, A.-Q. Li, Y. Fei and A.-J. Wang, *Electrochim. Acta*, 2013, **102**, 312-318.

53 B. Chen, D. Cheng and J. Zhu, *J. Power Sources*, 2014, **267**, 380-387.

54 D. H. Nagaraju and V. Lakshminarayanan, *J. Phys. Chem. C*, 2009, **113**, 14922-14926.

55 C. Koenigsmann, A. C. Santulli, K. Gong, M. B. Vukmirovic, W.-P. Zhou, E. Sutter, S. S. Wong and R. R. Adzic, *J. Am. Chem. Soc.*, 2011, **133**, 9783-9795.

56 Z. Chen, M. Waje, W. Li and Y. Yan, *Angew. Chem. Int. Ed.*, 2007, **46**, 4060-4063.

57 J. Prabhuram, T. S. Zhao, Z. X. Liang and R. Chen, *Electrochim. Acta*, 2007, **52**, 2649-2656.

58 Y. Kang and C. B. Murray, *J. Am. Chem. Soc.*, 2010, **132**, 7568-7569.

59 D. A. Gough and J. K. Leypoldt, *Anal. Chem.*, 1979, **51**, 439-444.

60 H. J. Kim, Y. S. Kim, M. H. Seo, S. M. Choi, J. Cho, G. W. Huber and W. B. Kim, *Electrochem. Commun.*, 2010, **12**, 32-35.

61 C. Koenigsmann, M. E. Scofield, H. Liu and S. S. Wong, *J. Phys. Chem. Lett.*, 2012, **3**, 3385-3398.

62 C. Koenigsmann, W.-p. Zhou, R. R. Adzic, E. Sutter and S. S. Wong, *Nano Lett.*, 2010, **10**, 2806-2811.

63 H. Liu, C. Koenigsmann, R. R. Adzic and S. S. Wong, *ACS Catal.*, 2014, **4**, 2544-2555.

64 H.-W. Liang, X. Cao, F. Zhou, C.-H. Cui, W.-J. Zhang and S.-H. Yu, *Adv. Mater.*, 2011, **23**, 1467-1471.

Captions

Fig. 1 TEM (A and B) and HR-TEM (C and D) images, and SAED pattern (E) of AuPt NNs. (F) XRD patterns of AuPt NNs (curve a), standard bulk Au (curve b) and Pt (curve c).

Fig. 2 HAADF-STEM-EDS elemental mapping images (A-C) and cross-sectional compositional line profiles (D) taken from AuPt NNs. Inset shows the respective HAADF-STEM image.

Fig. 3 TEM images of the AuPt products obtained without (A), and with 10 μL (B), 40 μL (C), and 80 μL (D) *N*-methylimidazole.

Fig. 4 Schematic illustration of the formation mechanism of AuPt NNs.

Fig. 5 (A) CV curves of AuPt NNs (curve a), Pt black (curve b), and Pt nanoparticles (curve c) modified electrodes in 0.5 M H_2SO_4 + 1.0 M methanol at a scan rate of 50 mV s^{-1}. (B) The corresponding mass activity and specific activity. (C) Chronoamperometric curves of AuPt NNs (curve a), Pt black (curve b), and Pt nanoparticles (curve c) modified electrodes in 0.5 M H_2SO_4 + 1.0 M methanol at the applied potential of 0.6 V.

Fig. 6 (A) ORR polarization curves of AuPt NNs (curve a), Pt black (curve b), Au

nanoparticles (curve c), and Pt nanoparticles (curve d) modified electrodes in O_2-saturated 0.1 M KOH at 10 mV s^{-1} with a rotation rate of 1600 rpm. (B) The comparison of the corresponding mass activity and specific activity at –0.6 V.

Fig. 7 (A) ORR polarization curves of AuPt NNs modified electrode in O_2-saturated 0.1 M KOH at 10 mV s^{-1} with different rotation rates (curve a-e): 100, 400, 900, 1600, and 2500 rpm. (B) The corresponding Koutecky-Levich plots at different potentials. (C) ORR polarization curves of AuPt NNs modified electrode before (curve a) and after (curve b) the accelerated durability test.

Figures

Fig. 1

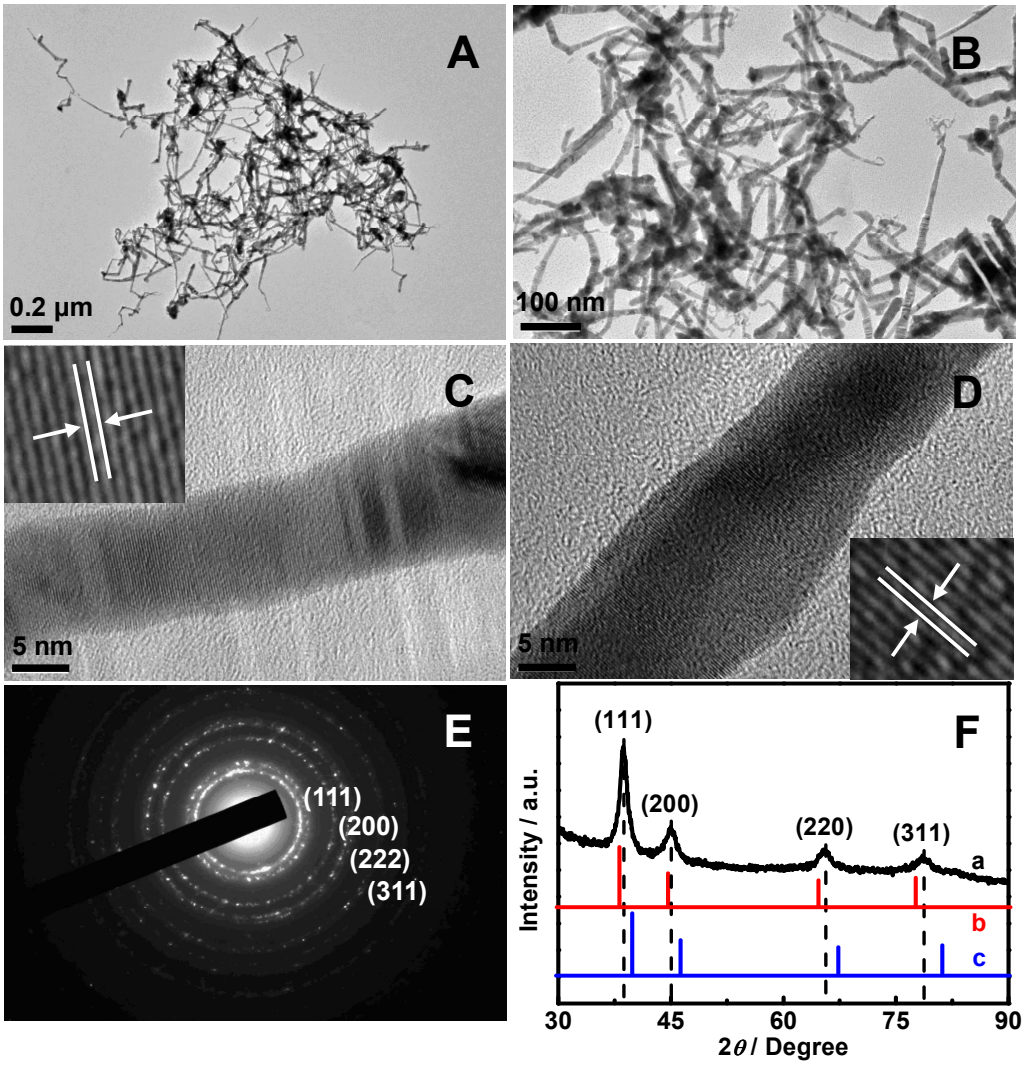

Fig. 2

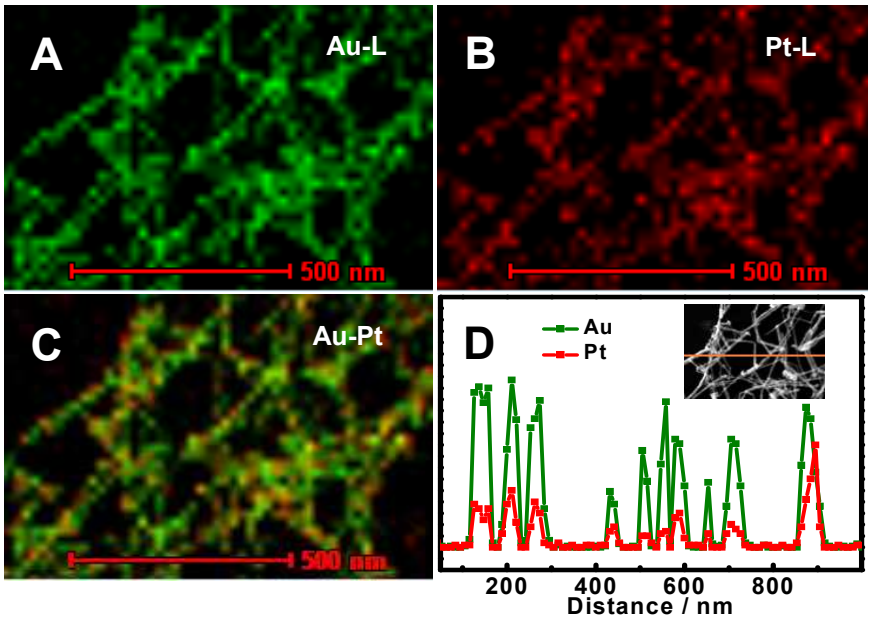

Fig. 3

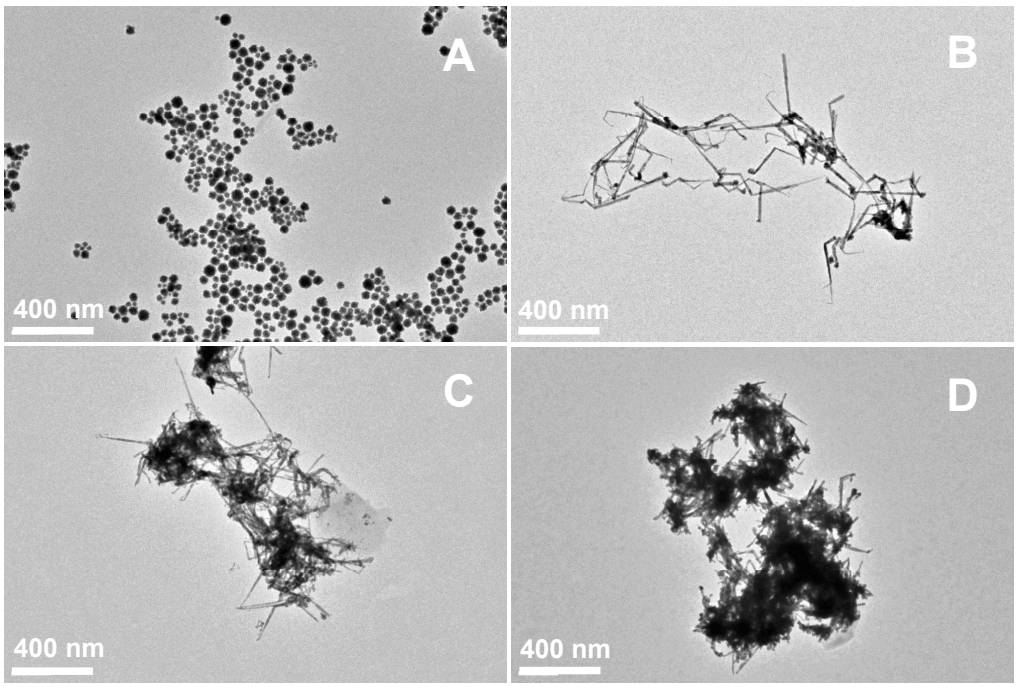

Fig. 4

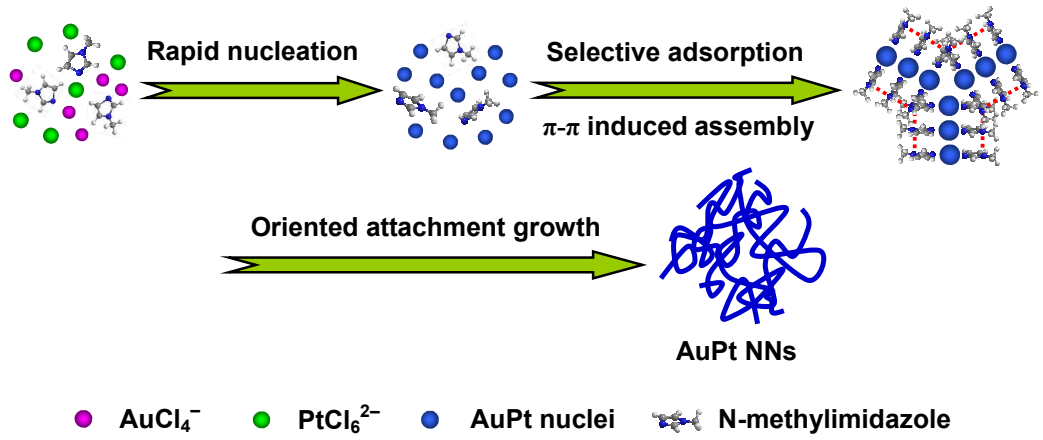

Fig. 5

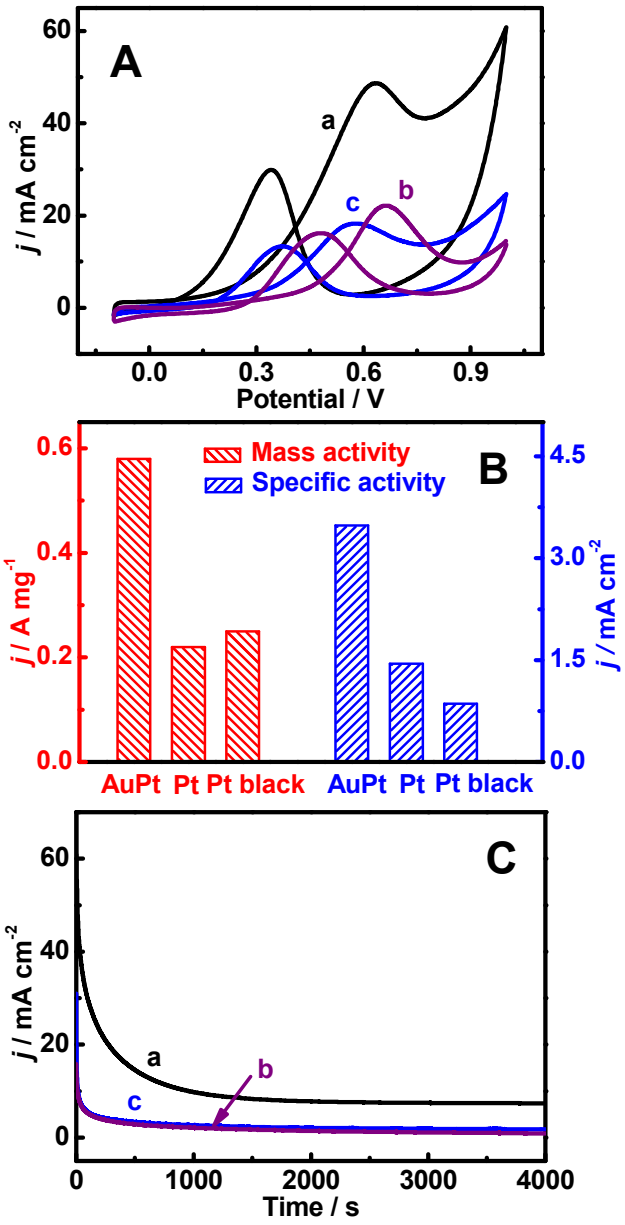

Fig. 6

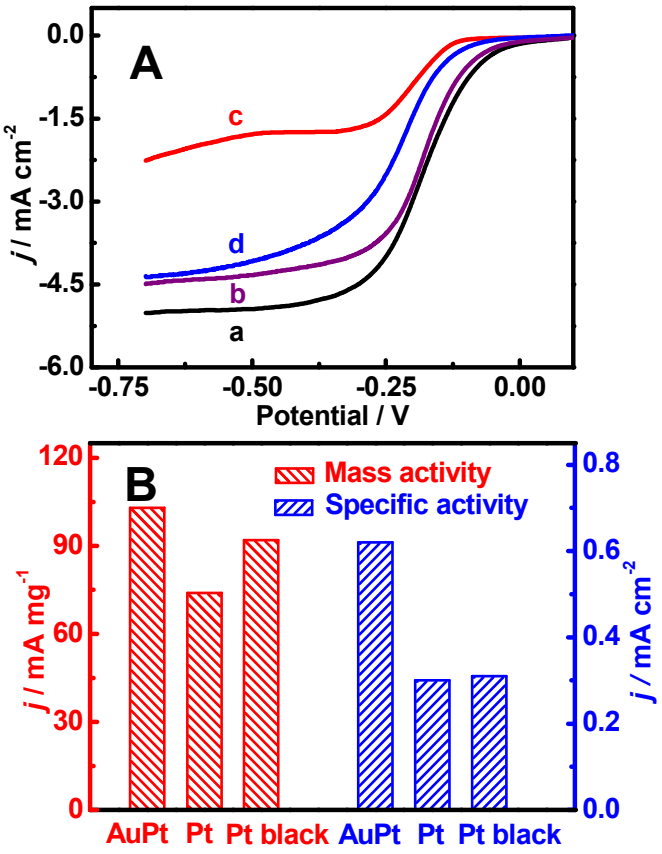

Fig. 7

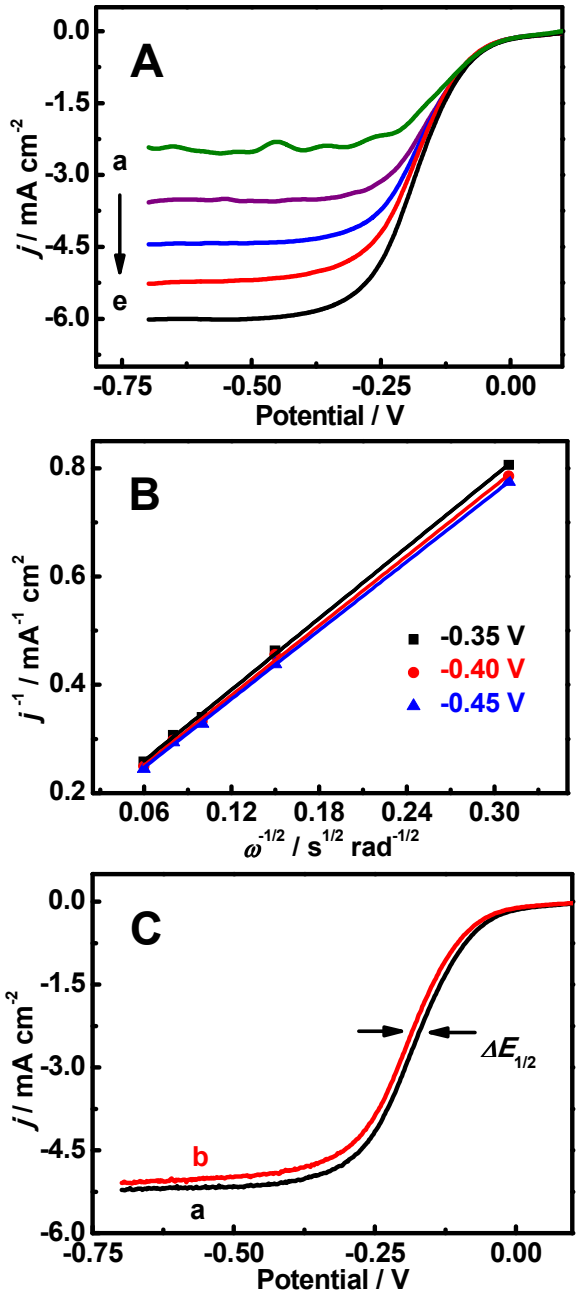

Graphical Abstract

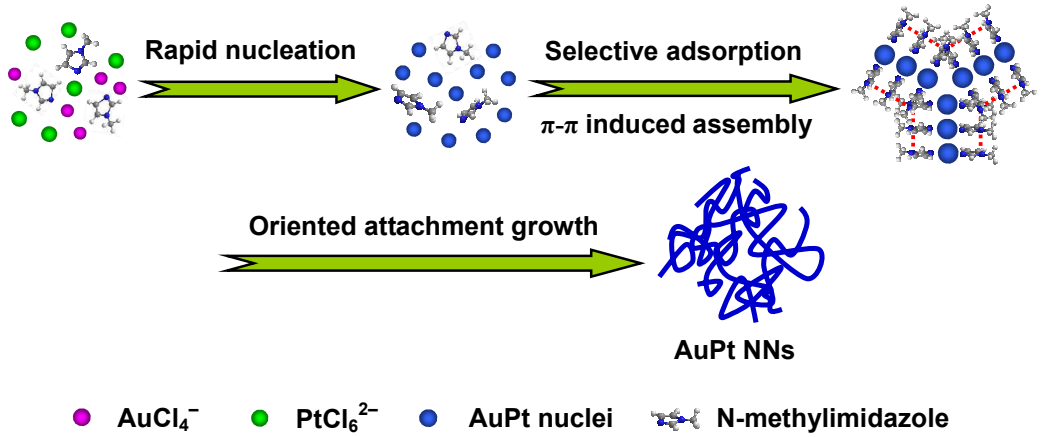

A rapid one-pot wet-chemical method was developed for large-scale preparation of surface-clean AuPt alloyed nanowire networks with the assistance of *N*-methylimidazole as a structure-directing agent and a weak stabilizing agent.